Volume 13
Number 20
28 May 2025
Pages 14425–15280

Journal of Materials Chemistry A

Materials for energy and sustainability

rsc.li/materials-a

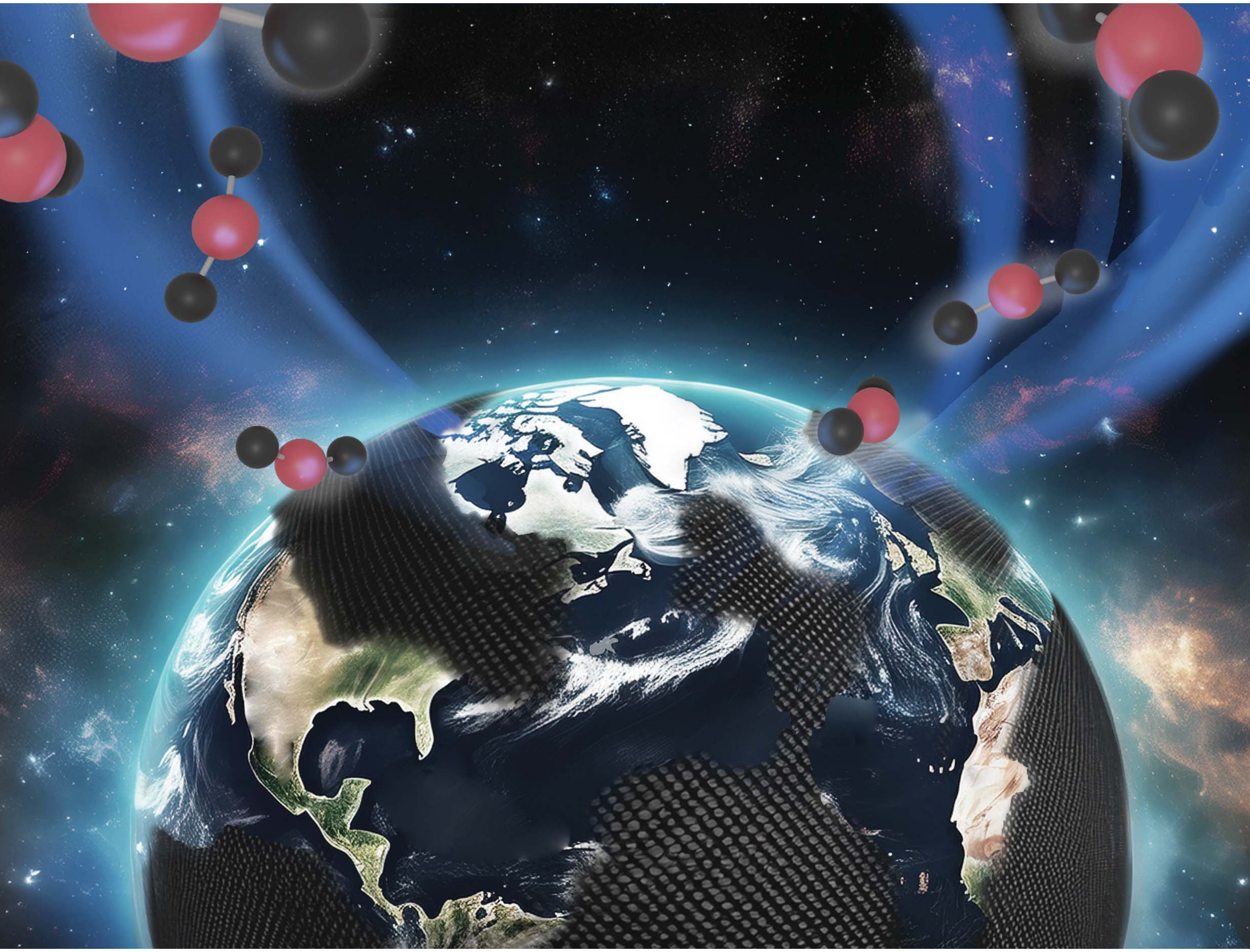

ISSN 2050-7488

ROYAL SOCIETY
OF **CHEMISTRY**

PAPER
Mantae Kim, Seul-Yi Lee, Soo-Jin Park *et al.*
Steam activation of pitch-based carbon fibers for increasing CO_2 adsorption behaviors

Journal of
Materials Chemistry A

ROYAL SOCIETY
OF CHEMISTRY

PAPER

View Article Online
View Journal | View Issue

Check for updates

Cite this: *J. Mater. Chem. A*, 2025, **13**, 14580

Steam activation of pitch-based carbon fibers for increasing CO_2 adsorption behaviors†

Choong-Hee Kim,[a] Mantae Kim, *[b] Jaein Lee,[c] Hokab Choi,[c] Seul-Yi Lee*[a] and Soo-Jin Park *[ad]

Received 18th January 2025
Accepted 19th February 2025

DOI: 10.1039/d5ta00486a

rsc.li/materials-a

Activated carbon fibers (ACFs) have attracted considerable interest as versatile adsorbents for gas separation, water treatment, and similar applications due to their high specific surface area, chemical stability, and robust mechanical properties. In this study, we synthesized ACFs using steam activation and systematically evaluated their CO_2 capture performance. The specific surface area of pitch-derived ACFs (SCF-*X*, where *X* is the activation temperature) increased significantly, reaching 2564 $m^2\ g^{-1}$ in SCF-900. Notably, SCF-800 exhibited the highest CO_2 adsorption capacity, emphasizing the role of micropores <0.73 nm in facilitating efficient CO_2 uptake at 273 K (4.32 mmol g^{-1}), while larger micropores <1.1 nm contributed to a maximum adsorption of 3.50 mmol g^{-1} at 298 K. Additionally, the adsorption kinetics were described by the pseudo-first-order model (R^2 > 0.99) across all temperatures (303, 313, and 323 K). This indicated that physisorption predominantly governs the process. Moreover, stable cyclic adsorption–desorption tests performed under simulated flue gas conditions (15% CO_2/85% N_2 at 313 K) demonstrated energy-efficient regeneration. These findings suggest that steam-activated ACFs are highly promising for CO_2 capture applications, offering advantages in terms of environmental sustainability, energy efficiency, and scalability.

1. Introduction

Global warming is accelerating, with the climate potentially undergoing more rapid changes than previously anticipated in the coming years. The global average temperature in January 2024 increased 1.6 °C above pre-industrial levels, surpassing the critical 1.5 °C threshold, as reported by the Copernicus Climate Change Service (C3S).[1–3] This concerning trend has raised alarms within the scientific community, which warns that sustained exceedances of this temperature limit could trigger irreversible and catastrophic consequences for the planet. To achieve global net-zero CO_2 emissions by 2050, an extensive range of carbon reduction and removal strategies is required. Key measures include scaling up renewable energy resources such as solar, wind, green hydrogen, and nuclear power, transitioning away from fossil fuels, promoting the widespread adoption of electric vehicles, enhancing afforestation efforts, and implementing carbon capture and storage technologies.[4–6]

The carbon capture and storage (CCS) strategy is a key approach for achieving long-term reductions in CO_2 emissions. To date, various CO_2 capture techniques, such as chemical absorption, physisorption, cryogenic distillation, direct air capture, mineral carbonation, and oxyfuel processes, have been extensively studied and reported.[7–9] Among these, physisorption using solid adsorbents has emerged as a particularly promising technology due to its cost-effectiveness, accessibility, environmental sustainability, and the stability of CO_2 adsorption–desorption cycles.[10] An effective solid adsorbent must possess the following characteristics: (i) high CO_2 adsorption capacity, (ii) appropriate kinetics to ensure efficient CO_2 capture under varying pressure and temperature conditions, (iii) stability over multiple adsorption–desorption cycles, particularly in real-world applications involving flue gas, and (iv) resistance to moisture and mechanical degradation.[11–13] The rapid kinetics of CO_2 adsorption–desorption is particularly crucial in industrial applications as they directly impact the cost efficiency and scalability of carbon dioxide capture processes.[14,15]

Activated carbon fibers (ACFs) are considered highly promising adsorbents for CO_2 capture because of their high specific surface areas, well-developed microporosity, cost-effectiveness, ease of production, and exceptional stability under humid conditions. Unlike polymer-based precursors that require additional activation steps, pitch naturally possesses a high fixed carbon content, enabling efficient pore development.[16,17] The chemical activation of ACFs involves impregnating carbon precursors with activating agents such as KOH, $ZnCl_2$, or

---

[a] Department of Chemistry, Inha University, Incheon 22212, Republic of Korea. E-mail: hm326000@naver.com; leesy1019@inha.ac.kr

[b] Aerospace Convergence Materials Center, Korea Institute of Ceramic Engineering and Technology, Republic of Korea. E-mail: ginggiscan@kicet.re.kr

[c] SG Safety Corporation, 28 Sinpyeong-ro, Pyeongtaek-si, Gyeonggi-do, Republic of Korea. E-mail: jaein.lee5@cj.net; hokab.choi@cj.net

[d] Department of Mechanical Engineering, College of Engineering, Kyung Hee University, Yongin 17104, Republic of Korea. E-mail: soojinpark@khu.ac.kr

† Electronic supplementary information (ESI) available. See DOI: https://doi.org/10.1039/d5ta00486a

H_3PO_4, followed by heat treatment at elevated temperatures (600–900 °C). This process induces pore formation through chemical reactions that remove non-carbon species, leading to the development of a highly microporous structure.[18,19] Among these reagents, KOH is widely used due to its ability to generate a well-developed pore network, but it poses environmental and handling concerns due to its corrosive nature.[20] $ZnCl_2$ and H_3PO_4 offer alternative activation routes with distinct pore structures, often favoring mesopore formation.[21,22] In contrast, physical activation is carried out by exposing carbon precursors to oxidizing gases such as CO_2, air, or steam at high temperatures (700–1100 °C). Steam activation, in particular, enhances microporosity by selectively removing less stable carbon structures while preserving the integrity of the porous network. This method eliminates the need for chemical reagents, making it a more environmentally friendly and scalable approach.[23,24]

The microporous structure of ACFs is crucial in enhancing their CO_2 capture performance due to the presence of narrow pores that are particularly favorable for CO_2 adsorption.[25–27] ACFs with an abundance of micropores with diameters less than 1 nm are expected to exhibit substantial CO_2 storage capacity, while the contribution of larger pores to the adsorption process is considered negligible.[28] Heo *et al.* produced PAN/PVDF-based ACFs through steam activation, exhibiting a specific surface area of 925 $m^2\ g^{-1}$, total pore volume of 0.404 $cm^3\ g^{-1}$, and micropore volume of 0.377 $cm^3\ g^{-1}$. The samples exhibited a remarkable CO_2 uptake capacity of 2.21 mmol g^{-1} at 298 K.[29] Presser *et al.* demonstrated that micropores smaller than 0.8 nm contribute the most to CO_2 uptake at 273 K and 1 bar.[30] Yan *et al.* reported porous polyimide-based activated carbon fibers with a specific surface area of 1156 $m^2\ g^{-1}$, total pore volume of 0.54 $cm^3\ g^{-1}$, and micropore volume of 0.44 $cm^3\ g^{-1}$. High CO_2 adsorption amounts of 6.2 and 4.4 mmol g^{-1} at 273 and 298 K were observed even with a lower specific surface area. They reported that the range of ultramicropore volume (<1 nm) played a key role in enhancing the CO_2 capacity.[31,32]

While numerous studies have explored the relationship between the pore size of activated carbons (ACs) and their CO_2 uptake capacity, most of these studies focus on reporting the equilibrium adsorption capacity at a specific temperature as a key criterion for identifying the most effective adsorbent.[33,34] Although the total CO_2 adsorption capacity is a useful metric for comparing different sorbents, this parameter may not fully reflect the performance in real-world cyclic processes. From a practical standpoint, assessing the working capacity—defined as the amount of CO_2 adsorbed at varying temperatures and/or low CO_2 partial pressures throughout a complete adsorption–desorption cycle—is a more appropriate approach for evaluating adsorbent efficiency.[35,36] Furthermore, a comprehensive understanding of adsorption kinetics and thermodynamics is crucial for developing adsorbents optimized for effective CO_2 capture in practical applications.

In this study, we synthesized pitch-derived ACFs using steam activation to assess their CO_2 capture performance. Furthermore, we systematically investigated the adsorption kinetics at various temperatures to determine key thermodynamic parameters, such as isosteric adsorption enthalpy, pseudo-first-order adsorption rate constants, and activation energy. Our findings revealed that micropores with sizes <0.73 nm and <1.1 nm were highly effective for CO_2 capture, yielding adsorption capacities of 4.32 and 3.50 mmol g^{-1} at 273 K and 298 K, respectively. Additionally, the stable cycling behavior observed during CO_2 adsorption–desorption under simulated flue gas conditions confirmed the predominance of physisorption, which is advantageous for energy-efficient regeneration processes. In summary, pitch-based ACFs synthesized through steam activation exhibited excellent adsorption capacity, indicating their potential as a sustainable green alternative for CO_2 capture.

2. Experimental

2.1. Materials and preparation of ACFs

The pitch precursor, with a softening point of 220 °C and a quinoline insoluble content of 2%, provided by DONGYANG ENVIRON-MENT Co., was spun into fibers using a melt-blown

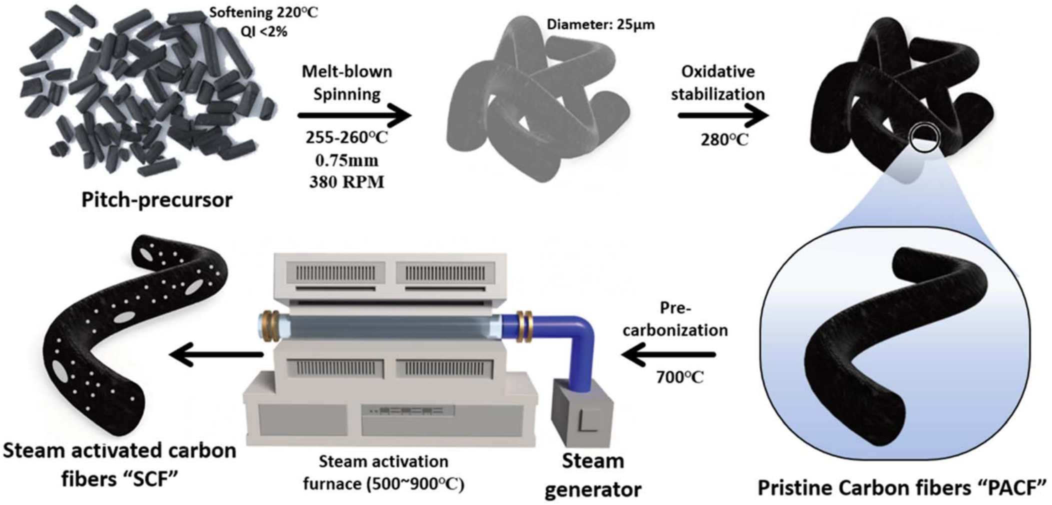

Fig. 1 Schematic of the preparation procedure of an ACF sample.

extruder. The spinning took place in the temperature range of 255–260 °C, utilizing a nozzle with a diameter of 0.75 mm at 380 rpm, yielding pitch fibers with a diameter of approximately 25 μm. These fibers underwent oxidation stabilization, pre-carbonization, and activation to produce ACFs. Oxidation stabilization was conducted by heating the fibers to a temperature 40–60 °C above the softening point of the pitch and maintaining it for 1 hour. Subsequently, pre-carbonization and activation were carried out sequentially in a tube furnace under a nitrogen (N_2) atmosphere. During the pre-carbonization stage, the stabilized pitch fibers were heated to 700 °C at a rate of 10 °C min^{-1} and held at this temperature for 1 h. For activation, physical activation was utilized, with steam being quantitatively supplied using a steam generator (E-1500, Cellkraft, Sweden) and a mass flow controller to regulate the steam flow rate. Physical activation was conducted at 500–700 °C for 1 h in a tube furnace under N_2 flow. The resulting samples were labeled as SCF-*X*, where "*X*" represents the temperature. A schematic of the synthesis route is shown in Fig. 1.

2.2. Characterization

The as-prepared ACF samples were characterized by a range of analytical techniques, the full details of which are provided in the ESI.†

3. Results and discussion

3.1. Morphological and structural properties

To clarify the impact of steam-assisted physical activation on the morphology of SCF samples, scanning electron microscopy (SEM) was conducted, as shown in Fig. 2. A significant morphological disparity between PACF (non-activated ACF) and SCF (steam-activated ACF) samples is clearly visible in the SEM images. The non-activated PACF sample exhibits densely packed structures with a smooth surface, while the SCF samples exhibit pronounced pore formation. Steam activation was performed under inert conditions at temperatures above 600 °C to prevent oxidative degradation of the porous carbon structure.[37,38] During this process, steam molecules interact with the carbon matrix, leading to the expansion of pre-existing ultramicropores and the generation of new ones. With increasing activation temperature, a more uniform distribution of pores emerges across the carbon surface, and thinner carbon layers become evident in the SCF samples. These observations indicate that steam gradually infiltrates the ACF channels throughout the activation process, causing the carbon layers to expand and etch, thereby forming well-defined pore structures.

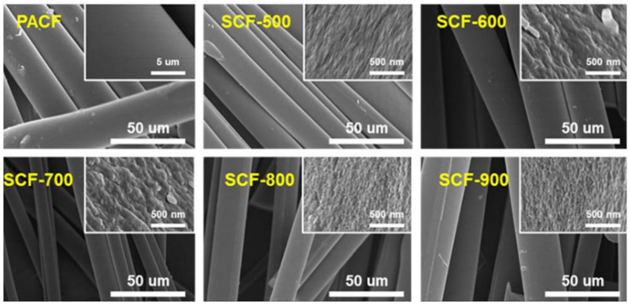

Fig. 2 High-resolution scanning electron microscopy image of the PACF and SCF samples.

The steam-activation mechanism to produce ACFs is outlined as follows:[39]

$$C^* + H_2O \rightarrow C{\cdot}H_2O \tag{1}$$

$$C{\cdot}H_2O \rightarrow H_2 + C{\cdot}O \tag{2}$$

$$C{\cdot}O \rightarrow CO \tag{3}$$

$$C^*H_2 \rightarrow C{\cdot}H_2 \tag{4}$$

To investigate the microcrystalline characteristics of the samples, X-ray diffraction (XRD) patterns were analyzed, as shown in Fig. 3(a). The XRD pattern of PACF exhibits characteristic carbon fiber peaks at $2\theta = 22°$ and 44°, corresponding to the C (002) and C (100, 101) planes, respectively.[40] In contrast to the diffraction angle of 26° of the C (002) peak in graphite crystallites, the 002 peaks in the prepared-ACF samples are observed at approximately 23°, indicating significant differences in the crystallite structure compared to that of graphite. Furthermore, with increasing activation temperature, the ACF samples show broader C (002) diffraction peaks, indicating reduced crystallinity due to the formation of highly disordered structures and an abundance of defects.

The microcrystalline graphitic structures of the samples were further analyzed using Raman spectroscopy, and the corresponding spectra are shown in Fig. 3(b). Two characteristic peaks, the D-band and G-band, appeared at approximately 1350 and 1580 cm^{-1}, respectively. The D-band is typically attributed to vibrations of carbon atoms with dangling bonds, indicating the presence of disordered and defective graphite. In contrast, the G-band is associated with the stretching of the carbon–

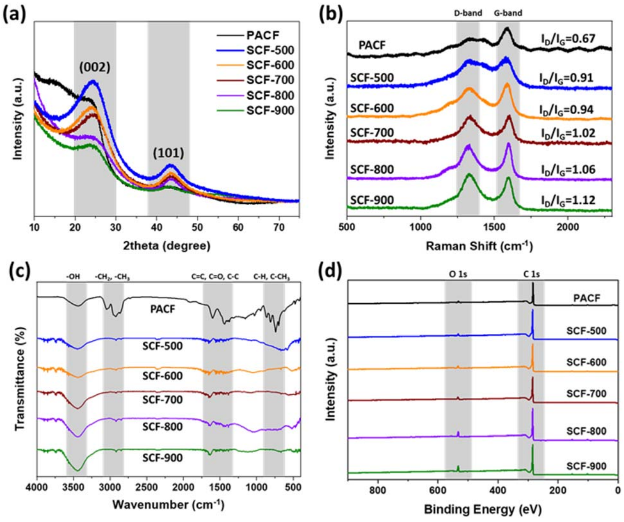

Fig. 3 (a) XRD patterns, (b) Raman spectra, (c) FT-IR spectra, and (d) XPS survey scan of the PACF and SCF samples.

carbon bonds in a hexagonal, two-dimensional lattice, characteristic of ordered graphite structures.[14] Notably, the intensity of the D-band peak progressively increases up to SCF-900, while that of the G-band remains largely unchanged. The degree of disorder in carbon-based materials is commonly evaluated by calculating the intensity ratio of the D-band to the G-band (I_D/I_G).[41] In this study, the SCF-900 sample exhibited the highest I_D/I_G ratio (1.12), indicating a highly disordered, amorphous structure. Thus, we can assume that the activation affects the sp^3 bonds and not the sp^2 bonds, and ACF becomes more amorphous as the activation temperature increases.

Fourier-transform infrared (FT-IR) spectroscopy was used to identify the functional groups present in the ACF samples, as shown in Fig. 3(c). The FT-IR spectrum of PACF exhibited a broad shoulder at 3450 cm^{-1}, corresponding to the stretching vibrations of hydroxyl groups (–OH). A distinct band at 2655 cm^{-1} was attributed to the stretching vibrations of hydrocarbon groups ($-CH_2$ and $-CH_3$). Furthermore, the band at 1625 cm^{-1} was associated with alkane (C–C), alkene (C=C), and carbonyl (C=O) groups. These spectral characteristics are consistent with the standard peaks reported in previous studies.[42] Similarly, the FT-IR spectra of the activated SCF samples exhibited peaks at approximately 3450 cm^{-1}, indicating the presence of hydroxyl groups (–OH), while the peaks at 2655 cm^{-1} were attributed to the $-CH_2$ and $-CH_3$ groups. The band at 1625 cm^{-1} was once again linked to alkane, alkene, and carbonyl groups.[43] These results demonstrate a comparable trend to that observed in the PACF samples. Importantly, with increasing activation temperature, there was a gradual increase in the peak intensity, suggesting that higher activation temperatures facilitate the incorporation of several oxygen functional groups on the surface.

The elemental and surface chemical compositions of the samples were analyzed using elemental analysis (EA) and X-ray photoelectron spectroscopy (XPS), respectively, with the results summarized in Table S1.† The EA data indicated that PACF consisted of 92.9 wt% carbon, 3.3 wt% oxygen, and 2.0 wt% hydrogen. Following physical activation, SCF contained 91.4–92.5 wt% carbon, 4.1–5.2 wt% oxygen, and 1.4–1.9 wt% hydrogen. A detailed quantitative XPS survey is provided in Fig. 3(d), showing a high carbon content of 90.7–96.2 at% and a moderate oxygen content of 3.8–7.2 at% in the ACF samples. Additionally, with increasing activation temperature, the total oxygen content increases from 3.6% to 7.2%. These findings are consistent with the bulk EA, demonstrating a correlation between the surface and bulk chemical compositions.[44,45]

3.2. Textural properties and CO_2 adsorption capacities

To assess the textural properties, N_2 adsorption–desorption isotherms and pore size distributions were obtained using non-local density functional theory (NLDFT), as shown in Fig. 4(a and b), with detailed textural characteristics summarized in Table 1. The isotherms of the prepared samples demonstrated a sharp increase in the low-pressure region ($P/P_0 < 0.01$), which is characteristic of a type I isotherm according to the International Union of Pure and Applied Chemistry (IUPAC) classification, indicating the predominant microporosity of the SCF samples.[46] Specifically, the SCF samples activated at relatively low temperatures (SCF-500, SCF-600, SCF-700, and SCF-800) exhibit no hysteresis, confirming their potential as ideal microporous materials. However, a small type H4 hysteresis loop was observed in SCF-900 within the P/P_0 range of 0.8–0.99 (Fig. S2†), associated with a higher temperature of steam activation.[47] This small hysteresis indicates the presence of a highly porous structure with a limited number of mesopores, facilitating gas uptake through capillary condensation. These results emphasize the crucial role of steam as a porogen in forming and enhancing microporous networks.[48]

To date, substantial literature has emerged on carbon fiber-derived ACFs, indicating a growing interest in utilizing carbon fibers for various applications. Tsuchiya *et al.* utilized $ZnCl_2$ as an activating agent to produce ACFs with a specific surface area (S_{BET}) of 1197 $m^2\ g^{-1}$ and a total pore volume (V_{total}) of 1.08 $cm^3\ g^{-1}$.[49] Abedi *et al.* fabricated asphaltene-derived ACFs through KOH activation, achieving an S_{BET} of 2290 $m^2\ g^{-1}$ and a V_{total} of 1.27 $cm^3\ g^{-1}$, which are suitable for supercapacitor applications.[50] Similarly, García-Mateos *et al.* demonstrated H_3PO_4-activated lignin-derived ACFs with a moderate S_{BET} of 2340 $m^2\ g^{-1}$ and a V_{total} of 0.97 $cm^3\ g^{-1}$, which can be optimized for supercapacitor electrodes.[51] In contrast, Choi *et al.* produced coal tar pitch-derived ACFs through physical activation (using water and CO_2), yielding a relatively lower S_{BET} of 1233 $m^2\ g^{-1}$ and a V_{total} of 0.50 $cm^3\ g^{-1}$ compared to other studies.[52] As demonstrated in the aforementioned studies, both chemical and physical activation agents have been predominantly used to synthesize microporous carbons with well-developed structures, leading to ACFs that typically exhibit only moderate textural properties. In contrast, our study achieved a significantly higher S_{BET} of 2564 $m^2\ g^{-1}$ and an enhanced V_{total} of 1.110 $cm^3\ g^{-1}$ for SCF-900.

The CO_2 adsorption isotherms of the ACF samples synthesized in this study were obtained at three different temperatures (273, 283, and 298 K) and at 1 bar to evaluate the adsorption kinetics (Fig. 4(c and d) and Table 2). The samples demonstrated CO_2 adsorption capacities ranging from 3.33 to 4.32 mmol g^{-1} at 273 K, 2.46 to 3.94 mmol g^{-1} at 283 K, and 2.01 to 2.32 mmol g^{-1} at 298 K. As expected, the adsorption capacities decrease progressively with increasing temperature, indicating that higher kinetic energy at elevated temperatures disrupts the van der Waals forces between the CO_2 molecules and solid adsorbents. This behavior is characteristic of an exothermic adsorption process, which limits the potential for high CO_2 adsorption at elevated temperatures.[53] Moreover, despite SCF-800 having relatively lower S_{BET} (1910 $m^2\ g^{-1}$) and V_{total} (0.859 $cm^3\ g^{-1}$) compared to SCF-900 (S_{BET} of 2564 $m^2\ g^{-1}$ and V_{total} of 1.110 $cm^3\ g^{-1}$), its highest CO_2 adsorption capacity of 4.32 mmol g^{-1} at 273 K exceeds that of SCF-900, which has a CO_2 adsorption capacity of 3.43 mmol g^{-1}. The correlation between the CO_2 adsorption capacity and S_{BET} indicates a weak correlation, with R^2 values between 0.01 and 0.06, as shown in Fig. 4(f). These results suggest that the contribution of S_{BET} to the CO_2 adsorption capacity is minimal at all tested temperatures.

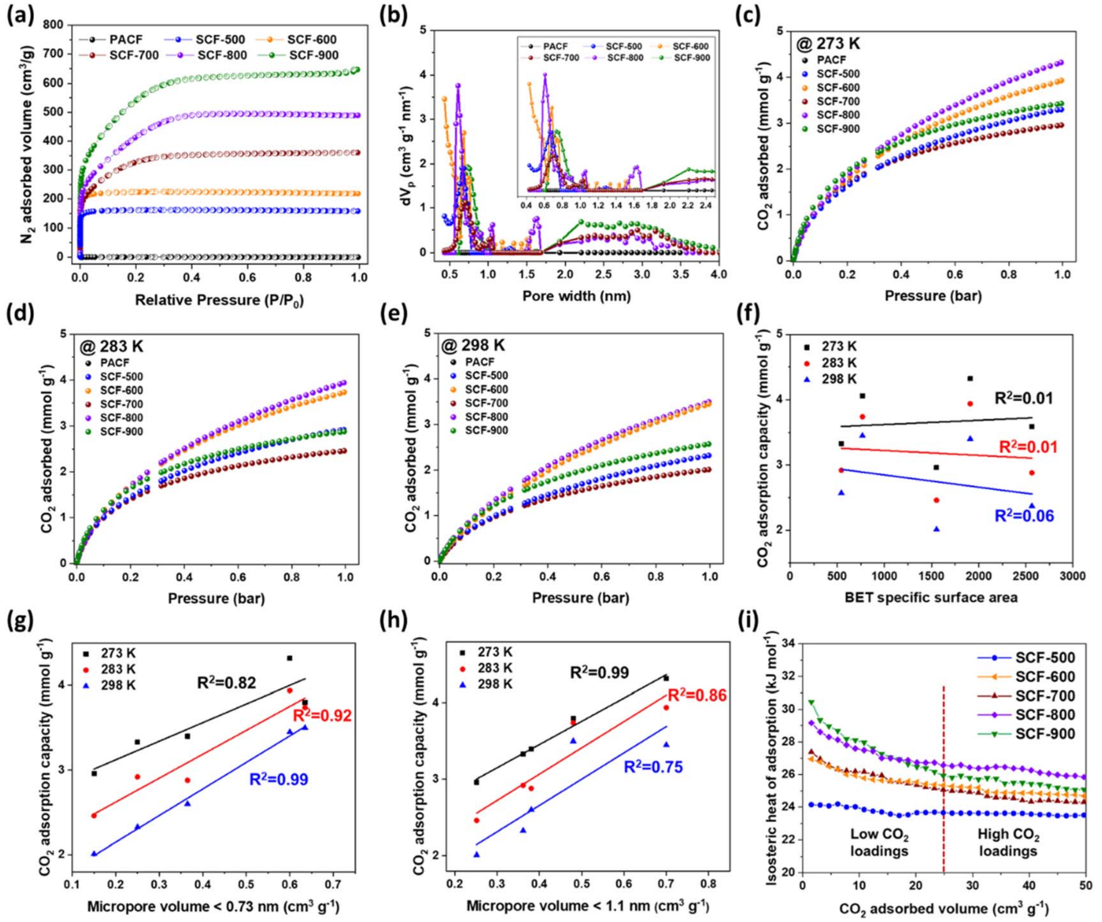

Fig. 4 (a) N_2 adsorption–desorption isotherms of the prepared samples at 77 K; (b) pore size distribution; (c–e) CO_2 adsorption–desorption isotherms at 273, 283, and 298 K, and the correlations between the CO_2 adsorption capacity and textural properties at different temperatures: 273, 283, and 298 K; (f) BET specific surface area with different pore size ranges less than (g) 0.73 and (h) 1.1 nm; (i) isosteric heat of adsorption for the prepared samples.

Table 1 Textural properties of the prepared samples

Sample	$^aS_{\mathrm{BET}}$ (m^2 g^{-1})	$^bV_{\mathrm{total}}$ (cm^3 g^{-1})	$^cV_{\mathrm{micro}}$ (cm^3 g^{-1})	$^dV_{\mathrm{meso}}$ (cm^3 g^{-1})
PACF	8	0.006	0.006	—
SCF-500	543	0.395	0.283	0.112
SCF-600	767	0.448	0.357	0.091
SCF-700	1552	0.783	0.299	0.484
SCF-800	1910	0.859	0.331	0.528
SCF-900	2564	1.110	0.481	0.629

[a] S_{BET}: specific surface area computed using the BET method. [b] V_{total}: total pore (0–50 nm) volume determined from the NLDFT method. [c] V_{micro}: micropore (0–2 nm) volume determined from the NLDFT method. [d] V_{meso}: mesopore (2–50 nm) volume determined from the NLDFT method.

Numerous studies have demonstrated that finely tuned micropores, along with a high specific surface area and total micropore volume, are crucial for enhancing CO_2 adsorption capacity. Consistent with these findings, our data indicate that micropore volume has a stronger correlation with the CO_2 adsorption capacity,[54] as shown in Fig. 4(g and h). Notably, the highest R^2 value of 0.99 was observed for the relationship between the CO_2 adsorption capacity and micropores smaller than 0.73 nm at 298 K. Similarly, a strong correlation with an R^2 of 0.99 was found for micropores less than 1.1 nm at 273 K. These results suggest that sub-micropores, specifically those with sizes below 0.73 nm and 1.1 nm, play a crucial role in enhancing the CO_2 adsorption capacity at 298 K and 273 K,[14,55–57] respectively. Furthermore, these correlations imply that the optimal pore size for maximizing CO_2 adsorption varies with temperature. Additionally, smaller micropores are particularly effective at lower temperatures, as they enhance the interaction between the adsorbent surface and CO_2 molecules,

Table 2 CO_2 adsorption performances and isosteric heat of adsorption of as-fabricated samples

	CO_2 adsorption capacity (mmol g^{-1})			
Sample	273 K	283 K	298 K	ΔH_{ads} for CO_2 (kJ mol^{-1})
SCF-500	3.33	2.92	2.32	24.2
SCF-600	3.93	3.74	3.45	27.0
SCF-700	2.96	2.46	2.01	27.4
SCF-800	4.32	3.94	3.50	29.2
SCF-900	3.43	2.88	2.57	30.5

thereby increasing the adsorption capacity.[58] The comparable CO_2 adsorption capacities of SCF-600 and SCF-800 at 298 K can be attributed to their similar micropore volumes for pores smaller than 0.73 nm, with SCF-600 and SCF-800 having pore volumes of 0.59 cm^3 g^{-1} and 0.63 cm^3 g^{-1}, respectively. Similarly, at 273 K, the dominance of SCF-800 in CO_2 adsorption capacity can be attributed to its largest micropore volume (0.71 cm^3 g^{-1}) for pores smaller than 1.1 nm.

The isosteric heat of adsorption (ΔH_{ads}) indicates the bond strength between the adsorbate and the solid adsorbent, and it is calculated using the Clausius–Clapeyron equation as follows:[59]

$$\ln\left(\frac{P_2}{P_1}\right) = -\frac{\Delta H_{ads}}{R}\left(\frac{1}{T_2} - \frac{1}{T_1}\right) \quad (5)$$

where P_2 and P_1 denote $p(CO_2)$; R is the universal gas constant; and T_2 and T_1 are 298 and 313 K, respectively.[60]

The isosteric heat of adsorption, as calculated for the samples, ranges from 24.2 to 30.5 kJ mol^{-1} (refer to Fig. 4(i) and Table 2). The CO_2 adsorption mechanism for all samples is identified as physisorption, which is advantageous due to its energy efficiency. During the initial low CO_2 loading phase, SCF-900 exhibits the highest initial ΔH_{ads} value, likely due to the favorable interaction of CO_2 molecules with the micro- and mesopores, acting as effective binding sites. However, at higher CO_2 loading levels, SCF-900 experiences a significant decline in the ΔH_{ads} value, which is attributed to the scarcity of efficient pores necessary for sustained CO_2 adsorption, thereby impeding CO_2 retention on the carbon surface. In contrast, SCF-800 exhibits a relatively stable curve with only a slight reduction in ΔH_{ads}, suggesting an abundance of active sites and a high adsorption potential, which can be attributed to the presence of micropores with diameters between 0.73 and 1.1 nm.[20]

Tables S2 and S3† show the comparison of various adsorbents for specific surface area and CO_2 adsorption performances. We believe that our preparation method for ACFs had significantly contributed to the emergence of efficient pores for CO_2 adsorption, affording the highest CO_2 adsorbed amount of 3.50 mmol g^{-1} at 298 K among the various ACFs investigated.

3.3. Kinetic adsorption–desorption behaviour characterization by thermogravimetric analysis under flue gas

The CO_2 adsorption–desorption behavior of the SCF-800 sample was evaluated using thermogravimetric analysis (TGA) under simulated flue gas conditions (15% CO_2/85% N_2 at 313 K), as shown in Fig. 5(a). As expected, the CO_2 uptake initially increases and eventually reaches saturation. Owing to the relatively low heat of adsorption (ranging from 0 to 40 kJ mol^{-1}) for these samples, the adsorbed CO_2 molecules are readily desorbed when switching the gas flow between CO_2 and N_2, indicating the predominance of physisorption.[61] Notably, the sample recovered 99% of its original CO_2 uptake capacity after gas purging. The adsorption and desorption cycles were conducted over a 1 h period under similar conditions, demonstrating an adsorption capacity of 52.8 mg g^{-1} for SCF-800 under flue gas conditions. Furthermore, complete CO_2 desorption occurred at 313 K within 1 h, with no significant loss in performance over 10 cycles, indicating robust regeneration capability.

To explore the kinetics of CO_2 adsorption in more detail, we obtained time-dependent CO_2 adsorption isotherms for a representative sample (SCF-800) at different temperatures (303, 313, and 323 K) under atmospheric pressure using TGA (Fig. 5(b), eqn (S1) and (S2), and Table S4†). The experimental data were analyzed using pseudo-first-order and pseudo-second-order kinetic models. While both models determine the adsorption rate, the pseudo-first-order model is based on the availability of adsorption sites (eqn (S1)†), whereas the pseudo-second-order model assumes that the rate is directly proportional to the square of the number of adsorption sites (eqn (S2)†). The experimental data showed the best fit with the pseudo-first-order model across all temperatures, with R^2 values exceeding 0.99, strongly suggesting a physisorption-dominated CO_2 capture mechanism.[62,63] Additionally, activation energy serves as a key parameter for evaluating the CO_2 adsorption

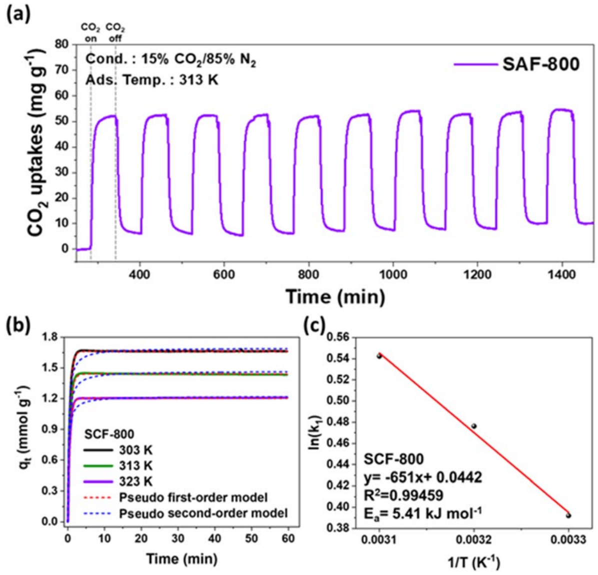

Fig. 5 (a) CO_2 adsorption–desorption profiles over 10 continuous vacuum swing adsorption cycles of SCF-800 under flue gas conditions (15% CO_2/85% N_2 gas mixture) at 313 K. (b) Kinetic study of CO_2 adsorption in SCF-800. (c) Pseudo first-order adsorption rate constant-based Arrhenius plot for estimating the activation energy.

efficiency of SCF-800. Lower activation energy values ($E_a = 0$–40 kJ mol^{-1}) typically indicate a physisorption-driven process. From the pseudo-first-order Arrhenius plot (Fig. 5(c)), an activation energy of 5.41 kJ mol^{-1} (eqn (S3)†) was calculated, indicating weak bonding between CO_2 molecules and the adsorbent surface, and highlighting the efficacy of steam activation in facilitating energy-efficient regeneration of ACFs.

4. Conclusions

In this study, pitch-based activated carbon fibers (ACFs) were synthesized *via* steam activation, demonstrating high CO_2 adsorption capacities of 4.32 mmol g^{-1} at 273 K and 3.50 mmol g^{-1} at 298 K. The enhanced adsorption performance was attributed to the presence of well-developed micropores (<0.73 nm and <1.1 nm), which played a key role in CO_2 uptake. The adsorption process followed a physisorption mechanism, confirmed by the isosteric heat of adsorption and pseudo-first-order kinetic model ($R^2 > 0.99$), with a low activation energy of 5.41 kJ mol^{-1}. Furthermore, SCF-800 exhibited stable adsorption–desorption performance over 10 cycles under simulated flue gas conditions (15% CO_2/85% N_2 at 313 K), highlighting its energy-efficient regeneration capability. Beyond CO_2 capture, the developed ACFs, with their high surface area, tunable porosity, and chemical stability, hold great potential for applications in gas storage and separation (*e.g.*, CH_4, H_2, or VOCs), water purification, energy storage devices, and catalytic support materials in environmental and industrial processes.

Data availability

The data supporting this article have been included as part of the ESI.†

Author contributions

Writing—original draft preparation: C.-H. K., J.-I. L., H.-K. C., S.-Y. L.; writing—review and editing: C.-H. K., S.-Y. L., S.-J. P; supervision: M.-T. K., S.-Y. L., S.-J. P. All the authors discussed and commented on the manuscript.

Conflicts of interest

There are no conflicts to declare.

Acknowledgements

This research was supported by Korea Energy (No. 2024-Research and Development in Field Technology, Yeongheung-01). This work was supported by the National Research Foundation of Korea (NRF) grant funded by the Korean government (MSIT) (No. 2023R1A2C1004109).

References

1 M. T. Mcculloch, A. Winter, C. E. Sherman and J. A. Trotter, *Nat. Clim. Change*, 2024, **14**, 171–177.
2 P. L. Yap, H. H. Nguyen, J. Ma, M. Gunawardana and D. Losic, *Sep. Purif. Technol.*, 2024, **348**, 127633.
3 N. Jones, *Nature*, 2023, **618**(7963), 20.
4 D. I. A. Mckay, A. Staal, J. F. Abrams, R. Winkelmann, B. Sakschewski, S. Loriani, I. Fetzer, S. E. Cornell, J. Rockstrom and T. M. Lenton, *Science*, 2022, **377**, eabn7950.
5 M. D. Mathew, *Prog. Nucl. Energy*, 2022, **143**, 104080.
6 H. H. Cho, V. Strezov and T. J. Evans, *Sustainable Mater. Technol.*, 2023, **35**, e00567.
7 F. Vega, F. M. Baena-Moreno, L. M. G. Fernandez, E. Portillo, B. Navarrete and Z. E. Zhang, *Appl. Energy*, 2020, **260**, 114313.
8 S. Yadav and S. S. Mondal, *Fuel*, 2022, **308**, 122057.
9 S. Paltsev, J. Morris, H. Kheshgi and H. Herzog, *Appl. Energy*, 2021, **300**, 117322.
10 M. S. Khosrowshahi, A. A. Aghajari, M. Rahimi, F. Maleki, E. Ghiyabi, A. Rezanezhad, A. Bakhshi, E. Salari, H. Shayesteh and H. Mohammadi, *Mater. Today Sustain.*, 2024, **27**, 100900.
11 J. Y. Lai, L. H. Ngu and S. S. Hashim, *Greenhouse Gases*, 2021, **11**, 1076–1117.
12 H. F. Hasan, F. T. Al-Sudani, T. M. Albayati, I. K. Salih, H. N. Hharah, H. S. Majdi, N. M. C. Saady, S. Zendehboudi, A. Amari and S. A. Gheni, *Process Saf. Environ. Prot.*, 2024, **182**, 975–988.
13 H. Si, J. Y. Yong, M. Yu, R. Y. Xie, N. Gao, X. Zhang and L. Jiang, *Fuel*, 2025, **380**, 133171.
14 C. H. Kim, S. Y. Lee and S. J. Park, *Green Chem.*, 2024, **26**, 1901–1909.
15 A. Mukhtar, S. Saqib, N. B. Mellon, M. Babar, S. Rafiq, S. Ullah, M. A. Bustam, A. G. Al-Sehemi, N. Muhammad and M. Chawla, *J. Nat. Gas Sci. Eng.*, 2020, **77**, 103203.
16 M. F. Hassan, M. A. Sabri, H. Fazal, A. Hafeez, N. Shezad and M. Hussain, *J. Anal. Appl. Pyrolysis*, 2020, **145**, 104715.
17 J. C. Liu, Y. P. Li, X. Y. An, C. Y. Shen, Q. Xie and D. C. Liang, *Environ. Res.*, 2022, **215**, 114197.
18 Y. X. Huang, E. N. Ma and G. J. Zhao, *Ind. Crops Prod.*, 2015, **69**, 447–455.
19 F. Mbarki, T. Selmi, A. Kesraoui and M. Seffen, *Ind. Crops Prod.*, 2022, **178**, 114546.
20 C. H. Kim, S. Y. Lee and S. J. Park, *J. CO2 Util.*, 2021, **54**, 101770.
21 M. Sevilla, N. Díez and A. B. Fuertes, *Chemsuschem*, 2021, **14**, 94–117.
22 E. D. Padilla-Martínez, S. K. Pérez-Buendía, R. López-Sandoval and C. E. Sánchez-Rodríguez, *J. Energy Storage*, 2023, **71**, 108115.
23 X. X. Liu, S. L. Zuo, N. N. Cui and S. S. Wang, *Carbon*, 2022, **191**, 581–592.
24 S. Mopoung and N. Dejang, *Sci. Rep.*, 2021, **11**, 13948.
25 S. Y. Lee and S. J. Park, *J. Colloid Interface Sci.*, 2013, **389**, 230–235.
26 N. Díez, P. Alvarez, M. Granda, C. Blanco, R. Santamaría and R. Menéndez, *Microporous Mesoporous Mater.*, 2015, **201**, 10–16.
27 C. H. Kim, S. Y. Lee, K. Y. Rhee and S. J. Park, *Adv. Compos. Hybrid Mater.*, 2024, **7**, 55.

28 Y. C. Chiang, C. Y. Yeh and C. H. Weng, *Appl. Sci.*, 2019, **9**, 1977.

29 Y. J. Heo, Y. F. Zhang, K. Y. Rhee and S. J. Park, *Composites, Part B*, 2019, **156**, 95–99.

30 V. Presser, J. McDonough, S. H. Yeon and Y. Gogotsi, *Energy Environ. Sci.*, 2011, **4**, 3059–3066.

31 S. G. Yan, R. J. Li, X. D. Fu, W. Y. Yuan, L. Jin, Y. F. Li, X. F. Wang and Y. G. Zhang, *Energy Fuels*, 2022, **36**, 11012–11024.

32 X. C. Ma, C. Q. Su, B. G. Liu, Q. D. Wu, K. Zhou, Z. Zeng and L. Q. Li, *Sep. Purif. Technol.*, 2021, **259**, 118065.

33 F. Raganati, R. Chirone and P. Ammendola, *Ind. Eng. Chem. Res.*, 2020, **59**, 3593–3605.

34 R. Chatterjee, B. Sajjadi, W. Y. Chen, D. L. Mattern, N. Hammer, V. Raman and A. Dorris, *Front. Energy Res.*, 2020, **8**, 85.

35 X. Z. Zhu, D. C. W. Tsang, L. Wang, Z. S. Su, D. Y. Hou, L. C. Li and J. Shang, *J. Cleaner Prod.*, 2020, **273**, 122915.

36 Z. Li, P. Liu, C. J. Ou and X. C. Dong, *ACS Sustainable Chem. Eng.*, 2020, **8**, 15378–15404.

37 Y. J. Zhang, Z. J. Xing, Z. K. Duan, M. Li and Y. Wang, *Appl. Surf. Sci.*, 2014, **315**, 279–286.

38 Y. Yoshikawa, K. Teshima, R. Futamura, H. Tanaka, A. V. Neimark and K. Kaneko, *J. Colloid Interface Sci.*, 2020, **578**, 422–430.

39 J. H. Lee, Y. J. Heo and S. J. Park, *Int. J. Hydrogen Energy*, 2018, **43**, 22377–22384.

40 M. Y. Hao, Z. Hu, Y. D. Huang, X. Qian, Z. P. Wen, X. F. Wang, L. Liu, F. Lu and Y. G. Zhang, *Composites, Part B*, 2022, **229**, 109468.

41 N. Chadha, R. Sharma and P. Saini, *Carbon Lett.*, 2021, **31**, 1125–1131.

42 H. I. Kim, W. Han, W. K. Choi, S. J. Park, K. H. An and B. J. Kim, *Carbon Lett.*, 2016, **20**, 39–46.

43 J. W. Yu, C. Chi, B. Zhu, K. Qiao, X. Cai, Y. Cheng and S. H. Yan, *Sci. Total Environ.*, 2020, **700**, 134412.

44 W. J. Wei, F. Wang, J. X. Yang, J. L. Zou, J. Li and K. Shi, *ACS Appl. Mater. Interfaces*, 2021, **13**, 6557–6565.

45 W. M. Qiao, L. C. Ling, Q. F. Zha and L. Liu, *J. Mater. Sci.*, 1997, **32**, 4447–4453.

46 M. Thommes, K. Kaneko, A. V. Neimark, J. P. Olivier, F. Rodriguez-Reinoso, J. Rouquerol and K. S. W. Sing, *Pure Appl. Chem.*, 2015, **87**, 1051–1069.

47 M. M. Rahman, M. Muttakin, A. Pal, A. Shafiullah and B. B. Saha, *Energies*, 2019, **12**, 4565.

48 H. D. Do and D. D. Do, *Chem. Eng. J.*, 2001, **84**, 295–308.

49 Y. Tsuchiya, Y. Yamaya, Y. Amano and M. Machida, *J. Environ. Manage.*, 2021, **289**, 112484.

50 Z. Abedi, D. Leistenschneider, W. X. Chen and D. G. Ivey, *Energy Technol.*, 2020, **8**, 2000538.

51 F. J. García-Mateos, R. Ruiz-Rosas, J. M. Rosas, E. Morallón, D. Cazorla-Amorós, J. Rodríguez-Mirasol and T. Cordero, *Sep. Purif. Technol.*, 2020, **241**, 116724.

52 B. K. Choi, J. K. Ko, S. J. Park and M. K. Seo, *Carbon Lett.*, 2017, **22**, 96–100.

53 J. M. Kolle, M. Fayaz and A. Sayari, *Chem. Rev.*, 2021, **121**, 7280–7345.

54 Z. Liu, Z. Zhang, Z. J. Jia, L. Zhao, T. T. Zhang, W. Xing, S. Komarneni, F. Subhan and Z. F. Yan, *Chem. Eng. J.*, 2018, **337**, 290–299.

55 J. Chen, J. Yang, G. S. Hu, X. Hu, Z. M. Li, S. W. Shen, M. Radosz and M. H. Fan, *ACS Sustainable Chem. Eng.*, 2016, **4**, 1439–1445.

56 S. W. Lee, Y. Lee, Y. Lee and H. Jo, *Appl. Therm. Eng.*, 2025, **261**, 125133.

57 Y. X. Yao, M. Y. Niu, M. C. Zi and D. Y. Chen, *Sep. Purif. Technol.*, 2025, **357**, 130151.

58 M. Sevilla, J. B. Parra and A. B. Fuertes, *ACS Appl. Mater. Interfaces*, 2013, **5**, 6360–6368.

59 S. Wang, Y.-R. Lee, Y. Won, H. Kim, S.-E. Jeong, B. W. Hwang, A. R. Cho, J.-Y. Kim, Y. C. Park and H. Nam, *Chem. Eng. J.*, 2022, **437**, 135378.

60 J. Serafin, K. Kiełbasa and B. Michalkiewicz, *Chem. Eng. J.*, 2022, **429**, 131751.

61 F. N. U. Huhe, J. King and S. S. C. Chuang, *Res. Chem. Intermed.*, 2023, **49**, 791–817.

62 C. Goel, S. Mohan and P. Dinesha, *Sci. Total Environ.*, 2021, **798**, 149296.

63 R. Han, Y. Wang, S. Xing, C. H. Pang, Y. Hao, C. F. Song and Q. L. Liu, *Chem. Eng. J.*, 2022, **450**, 137952.